RSC Advances

PAPER

View Article Online
View Journal | View Issue

Cite this: *RSC Adv.*, 2026, **16**, 21724

Rational construction of spinel cobaltite/MXene composites towards superior interfacial charge dynamics for advanced pseudocapacitors

Komal Ali Rao, *[a] Khizra Waheed,[a] Waqas Ahmad,[a] Nokhaiz Naeem,[b] Muhammad Imran Khan, [c] Muhammad Bilal,[d] Zahra Bayhan[e] and Muhammad Ehsan Mazhar[a]

The layered structure, large surface area, superior electrical conductivity, and outstanding chemical stability of MXenes make them attractive innovative electrode materials for supercapacitors. The incorporation of nanoparticles, particularly bi- and tri-metallic transition metal oxides, is commonly used to enhance the interlayer accessibility and improve the electrochemical performance. Among various MXenes, Nb_2CT_x stands out as an excellent candidate for supercapacitor applications because of its unique properties, which collectively facilitate rapid charge transport and efficient ion storage. A hydrothermal method was used in this work to fabricate a $MgCo_2O_4$/MXene nanocomposite. FTIR spectroscopy and XPS investigations revealed the chemical bonding, functional groups and various oxidation states, while XRD analysis confirmed the crystalline properties and phase uniformity of $MgCo_2O_4$/MXene. SEM coupled with EDX revealed irregular platelet-like nanoparticles distributed on the MXene layers and confirmed the elemental composition. The optimized electrode yielded an excellent specific capacitance of 1257.75 F g^{-1} at 1 A g^{-1} with a maximum cycling stability of 88.15% after 10 000 cycles. This research study illustrates a facile hydrothermal route for the synthesis of MXene-based nanocomposites with particles of controllable size for high-performance supercapacitor electrodes.

Received 9th April 2026
Accepted 10th April 2026

DOI: 10.1039/d6ra02980a

rsc.li/rsc-advances

1 Introduction

Global issues like climate alteration, ecological contamination, and limited resources are progressively risking human existence and growth. The main reasons for these issues are the common extraction and use of finite fossil fuels.[1–3] As the economy grows rapidly, traditional fossil fuels are constantly consumed, and environmental issues become worse. These problems have encouraged the researchers to search for renewable sources, such as wind, tidal and solar energy, that can replace fossil fuels and some other traditional energy resources.[4,5] Regarding the quick advancement of new power technology and transportation in the 21st century, the need for better energy storage solutions has further increased.[6,7] The ability of energy storage devices to overcome energy limitations has attracted a lot of research attention. Supercapacitors and Li-ion batteries have gained interest because of their distinct properties. Especially, supercapacitors have moderate energy density and high power density, while batteries have high energy density and moderate power density. To improve the energy density in supercapacitors, the capacitance of electrode materials has to be increased.[8–11] Supercapacitors, also known as ultracapacitors, are devices that exhibit exceptional capacitance, addressing the limitations of traditional batteries and dielectric capacitors by offering elevated energy storage density and high power density. They also have various other benefits, such as fast charge and discharge abilities, substantial power capacity, and functionality across a broad temperature spectrum.[12–14] Supercapacitors have two forms of devices for storing charges based on the mechanics of energy storage technologies that use non-faradic charge build up (EDLC), faradaic charge transfer (pseudo-capacitance), or a mixture of these two processes (hybrid capacitance).[15–17]

Mixed transition metal oxides or bi-metallic oxides exhibit greater specific capacitance, and their pseudocapacitive characteristics make them more suitable candidates for supercapacitor electrodes. Scientists have concentrated on various transition metal oxides, such as $ZnCo_2O_4$, $CuCo_2O_4$, $NiCo_2O_4$, and $MgCo_2O_4$, due to their capacity to create complex physical and chemical structures and produce remarkable synergistic

[a]*Institute of Physics Bahauddin Zakariya University, Multan-60800, Pakistan. E-mail: komalrao49@gmail.com*

[b]*Center for Advanced Studies in Physics, Government College University, Lahore, Pakistan*

[c]*Research Institute of Sciences and Engineering (RISE), University of Sharjah, Sharjah 27272, United Arab Emirates*

[d]*School of Engineering and Materials Science, Queen Marry University of London-E1 4NS, UK*

[e]*Department of Physics, College of Sciences, Princess Nourah Bint Abdulrahman University, P.O. Box 84428, Riyadh 11671, Saudia Arabia*

interactions among themselves.[18,19] Spinel cobaltites (XCo_2O_4, with X being Ca, Mg, or Ni) attract a lot of interest from researchers due to their affordability, safety, increased stability, and improved electrochemical characteristics.[20–22] Owing to their significant theoretical specific capacitance, materials like Mg and Co_3O_4 are considered to be the best practical choices among the several electrodes for transition metal oxides (TMOs).[23] The abundance of redox reactions in Co_3O_4 allows it to provide a comparatively large capacitance. The availability and high cost of cobalt limit its potential for energy storage applications. To solve this problem, researchers are substituting less costly metals, like Mg, Mn, Cu, Fe, Ni, and Zn, for some of the cobalt cations in the Co_3O_4 crystal structure.[24] The synergistic action of several metallic ions may cause cobalt-based bi-metallic transition metal oxides (BTMOs) to perform better than pure Co_3O_4 electrochemically and electrically.[25]

$MgCo_2O_4$ with a spinel structure is unique among BTMOs, because of its high theoretical specific capacitance (3122 F g^{-1}) and excellent electrochemical characteristics. Within the crystal arrangement of $MgCo_2O_4$, the magnesium ion is located in the tetrahedral position, while the cobalt ion resides in the octahedral position. Cobalt with different valence states is used in supercapacitors instead of elemental magnesium, which does not take part in redox reactions. The conductivity of magnesium is higher than that of cobalt. Replacing one of cobalt cations with magnesium is expected to improve the specific capacitance of Co_3O_4. In real-world applications, MCo_2O_4 (where M = Mg, Cu, Ni, and Fe) probably performs better than Co_3O_4 electrochemically.[26] For example, after a post-annealing procedure, Liu *et al.* identified the flower-shaped $CuCo_2O_4$ nanosheets and Co_3O_4 nanoflakes *via* a hydrothermal route. These nanomaterials, $CuCo_2O_4$ and Co_3O_4, exhibited an impressive capacitance of 1131 F g^{-1} in the range of 0–0.6 V and 664 F g^{-1} (0–0.6 V) at 1 A g^{-1}, respectively, with their capacities remaining at 79.7% and 68.0% at 10 A g^{-1} after 5000 cycles.[27] Yasun Y. Kannangara *et al.* created a nanostructured $NiCo_2O_4$ with a high density of defects, displaying 424 and 290 F g^{-1} of capacitance at 1.5 and 7.5 A g^{-1} of current density, respectively.[28] MoS_2@-$CuCo_2O_4$ exhibited capacitance of 640.2 F g^{-1} at 1 A g^{-1} retaining 78% after 10 000 cycles.[29] Liu *et al.* synthesized $MgCo_2O_4$ powders through a solvothermal method, utilizing anhydrous ethanol as the solvent and maintaining CO_2 pressure during the procedure. $MgCo_2O_4$ at 1 A g^{-1} generated at 16 MPa of CO_2 pressure reached a capacity of 296.4C g^{-1} (741 F g^{-1}, 0.1–0.5 V). However, at a current rate of 5 A g^{-1}, the specific capacity dropped to just 66.3% of its initial value.[30] Ghaziani *et al.* prepared $MgCo_2O_4$ nanofibers using sol–gel electrostatic spinning, which resulted in the nanofibers showing a C_s value of 84C g^{-1} (210 F g^{-1}, 0–0.4 V) when tested at 0.5 A g^{-1}.[31]

Researchers aim to improve the supercapacitor efficiency by structural engineering, including doping and combining with carbonaceous materials. Significant progress in low-dimensional materials like transition metal oxides, transition metal dichalcogenides, carbon-based materials, black phosphorus, and emerging MXenes has emphasized the importance of layered structures, high surface area, and electronic structure in developing advanced charge storage and fast ion conduction for next-generation supercapacitors. The integration of multifunctional 2D materials with pseudocapacitive compounds provides new insights for overcoming the limitations in cycling stability and ion conductivity, thereby facilitating the fabrication of advanced electrode materials for high-performance supercapacitors.[32–34] MXenes are two-dimensional transition metal carbides and nitrides that have recently emerged as promising candidates for electrochemical energy storage. MXenes are generally synthesized by selective etching of the A-layer from the layered $M_{n+1}AX_n$ (MAX) phases to obtain $M_{n+1}X_nT_x$ compounds, where T_x represents surface terminations group such as –F, –OH, and –O in MXenes.[35–37] MXene materials are highly appealing due to their distinctive stacked structure, abundant interface connections, improved electrical conductivity, hydrophilicity, and larger specific surface area for a range of electrochemical applications requiring energy storage.[38,39] For supercapacitors, the MXene has been utilized as a substrate for the composite electrode, incorporating different metal oxides such as vanadium oxide attached to $Ti_3C_2T_x$ (364 F g^{-1}),[40] $Ti_3C_2T_x$/$CuCo_2S_4$ (993C g^{-1} at 1 A g^{-1}),[41] and MXene/carbon nanotube@MnO_2 (221 F g^{-1}).[42]

Thus far, MXene research has been centered on $Ti_3C_2T_x$ due to its well-established synthesis routes. Nevertheless, MXene electrochemical behavior is greatly influenced by its structural configuration such that an increase in atomic layers corresponds to an increase in molecular weight and a decrease in theoretical specific capacity. Consequently, the materials with the M_2X composition are likely to have higher theoretical capacities than those of the M_3X_2 family, such as $Ti_3C_2T_x$. Among the family of MXenes, Nb_2CT_x is emerging as a promising material because of its exceptional chemical stability, outstanding electrical conductivity, zero bandgap, metallic character and more interlayer spacing which ultimately allows placement of discharge ions. These characteristics are further enhanced by the presence of surface termination groups (such as –O, –OH, and –F).[43,44] Although the Nb_2AlC MAX phase was reported in 2000, the discovery of Nb_2C MXenes through selective etching of Nb_2AlC in 2013 initiated extensive research on Nb_2C MXene materials. Since then, Nb_2C has demonstrated promising uses in solar energy conversion, batteries, supercapacitors, hydrogen/oxygen evolution, and other fields. Increasing space between layers and preventing reassembling are important research goals to enhance the effectiveness of MXene in energy storage applications.[45] The innovative layout of these composites addresses the drawbacks of both materials by utilizing the remarkable electronic conduction of Nb_2CT_x MXenes and high redox activity of $MgCo_2O_4$. It is anticipated that the synergistic effect of both oxides and MXenes improves the structural stability, accelerates the charge transfer kinetics, and boosts the overall electrochemical performance.

In this work, $MgCo_2O_4$/MXene nanocomposites were synthesized using a hydrothermal method because of their high capacity and redox reaction. The structural and electrochemical properties of composite materials were investigated in this research. This work advances the field of MXene-based hybrid materials for introducing a unique electrode material for supercapacitor and efficient hydrogen/oxygen evolution reaction applications.

2 Research laboratory methods

2.1 Materials

Cobalt(III) nitrate ($Co(NO_3)_2$, 99% purity), magnesium(II) nitrate ($Mg(NO_3)_2$, 99% purity), hydrofluoric acid (HF, 98% purity) and MAX (Nb_2AlC, 99% purity) were all obtained from Sigma Aldrich. Ethanol and distilled H_2O (99.9% purity) were obtained from local laboratories and no other procedure were essential to clean the materials because all of the materials used in the experiment were analytical quality.

2.2 MXene (Nb_2CT_x) preparation

Here, high-yield Nb_2CT_x MXene sheets were produced by selectively etching the niobium aluminum carbide (Nb_2AlC) powder to remove the Al atoms, as depicted in Fig. 1. Immediately, 10 mL of 40% concentrated HF solution was combined with 1 g of Nb_2AlC powder, which was stirred at 400 rpm for 24 hours at 27 °C. The resultant material was centrifuged many times (at 4500 rpm), using ethanol and double-distilled (DDI) water to achieve a pH of 6 in order to generate fine MXene layers. After that, the precipitate was placed for 8 hours at 60 °C in an oven. After HF etching, the Nb_2CT_x MXene with the characteristic accordion-like morphology is formed due to the selective etching of the Al layer from the Nb_2AlC MAX phase, as seen in Fig. 1. This is in accordance with previous studies on the production of MXene sheets.[46]

Further, precipitate was placed for 8 hours at 60 °C in an oven. As seen in Fig. 1, we eventually obtain the uniform 2D Nb_2CT_x MXene sheets.

2.3 Preparation of $MgCo_2O_4$/MXene (Nb_2CT_x) composites

The hydrothermal process was used to prepare $MgCo_2O_4$/MXene (Nb_2CT_x). Initially, 0.2 mol of $Co(NO_3)_2$ and 30 mL of distilled water were mixed with 0.1 mol of Mg $(NO_3)_2$ and magnetically stirred for 1 hour. Then, while continuously stirring, 5 mL hydrous solution of 100 mg of synthesized MXene (Nb_2CT_x) was added dropwise to the precursor solution. In another beaker, 0.4 mol of urea and 0.8 mol of ammonium fluoride were dissolved in 20 mL distilled water and added slowly dropwise into the stirred precursor solution. Ammonium fluoride was added as a mineralizer and etching agent. It facilitates the uniform nucleation of $MgCo_2O_4$ nanoparticles on the MXene surface and improves the dispersion and interfacial interaction between MXenes and spinel oxide. The solution was stirred for 30 minutes to complete mixing until the pH reached 7–8. The resultant solution was stirred, put into a stainless-steel autoclave lined with Teflon and then heated to 180 °C for 12 hours in an electric oven. The precipitate was collected by centrifugation at 4000 rpm for 20 minutes after naturally cooling to room temperature. To remove impurities, it was continuously washed with DI water and ethanol, respectively. The collected precipitates were dried for 12 hours at 80 °C in an oven. The produced powder was obtained and annealed in a muffle furnace for 6 hours at 550 °C under a N_2 atmosphere to prevent oxidation and decomposition of the Nb_2C MXene, thereby improving its structural and functional qualities. The synthesized sample was named $MgCo_2O_4$/MXene (MCO/MX), as illustrated in Fig. S1. The same method was employed for the synthesis of $MgCo_2O_4$ (MCO) composites, except the addition of the MXene solution.

2.4 Preparation of the working electrode

Three electrode systems were employed to evaluate the electrochemical performance. To fabricate the working electrode (WE), a nickel foam (NF) was cut into 2 × 2 cm^2 pieces and subjected to ultrasonic cleaning in ethanol, 10% HCl, and distilled water consecutively. Finally, it was dried at 60 °C in an oven for 60 minutes. For the fabrication of the electrodes, active material $MgCo_2O_4$/MXene (50 wt%), carbon black (25 wt%), and PVDF binder (25 wt%) were mixed with 80 μL of *N*,*N*-

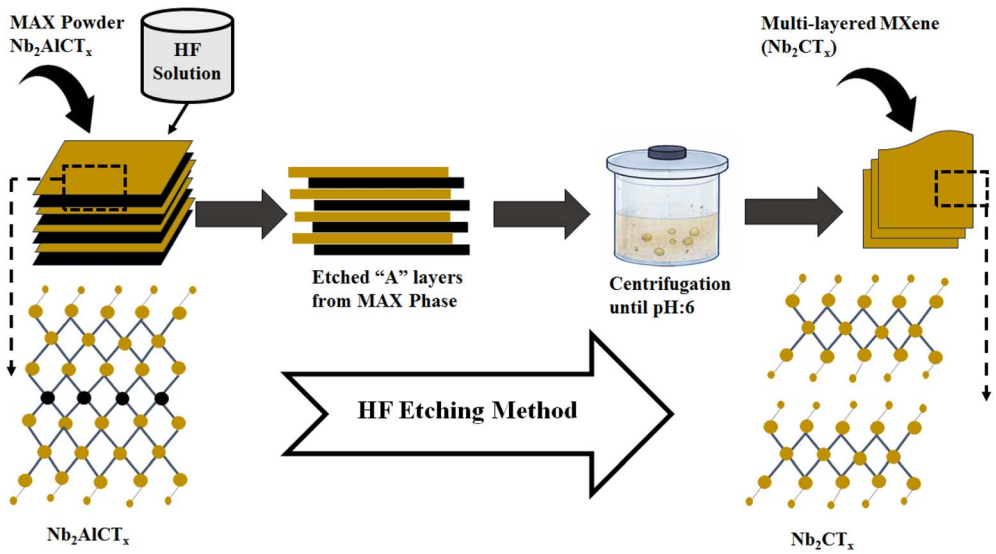

Fig. 1 Schematic of the multilayered (accordion-like) Nb_2CT_x MXene obtained from Nb_2AlC (MAX).

dimethylformamide solvent. Afterward, the mixture was stirred at 150 rpm for 2 hour and drop-cast onto the NF substrate. Finally, it was dried at 60 °C in an oven for 24 hours. The loading mass of the active material was 3 mg per electrode. Both electrodes were prepared in the same manner and utilized to investigate the electrochemical characteristics of supercapacitors.

3 Results and discussion

3.1 Structural characterization

3.1.1 XRD and FTIR spectroscopy. The X-ray diffraction (XRD) measurements were used to determine the phase homogeneity and structural characteristics of the prepared sample $MgCo_2O_4$. The X'Pert Highscore software was used to index the diffraction patterns. The XRD profiles of the synthesized $MgCo_2O_4$ are displayed in Fig. 2(a), which depicted diffraction peaks at angle 2θ values of 31.05°, 36.84°, 38.20°, 44.69°, 55.16°, 58.82°, 64.90° and 73.99° that can be indexed to the (220), (311), (222), (400), (422), (511), (440) and (620) crystal planes of cubic $MgCo_2O_4$ from JCPDS #(00-002-1073), with lattice parameters, $a = 8.1006$ Å, $b = 8.1006$ Å, and $c = 8.1006$ Å. The prominent and well-defined peaks of $MgCo_2O_4$ in the XRD pattern suggest its high level of crystallinity. In the case of $MgCo_2O_4$/MXene, Fig. 2(b) shows the diffraction peak at angle 2θ values of 31.22°, 36.87°, 38.28°, 44.63°, 55.19°, 58.89°, 64.98° and 73.95° that can be indexed to the (220), (311), (222), (400), (422), (511), (440) and (620) crystal planes of cubic $MgCo_2O_4$ from JCPDS #(00-002-1073). The diffraction peak at a 2θ value of 9.65° can be indexed to the (002) crystal plane, confirming the incorporation of carbon-based materials within the composite sample. The integration of the MXene phase is confirmed by the diffraction peak at 2θ values of 50.44° and 66.53°, which may be indexed to the (102) and (103) hexagonal niobium carbide (Nb_2CT_x) crystal planes from JCPDS #(00-015-0127). The XRD pattern of the $MgCo_2O_4$/MXene composites indicates the successful synthesis by showing distinctive peaks for $MgCo_2O_4$, MgO, and Nb_2CT_x. Additionally, the crystallite size of the prepared $MgCo_2O_4$ and $MgCo_2O_4$/MXene was measured by the Scherrer method using the following expression:[47,48]

$$D(\text{nm}) = K\lambda/\beta \cos \theta, \quad (1)$$

where λ is the wavelength of X-ray radiation and has a value of 0.15406 Å, K is a constant and has a value of 0.9, D is the size of the crystallite in nanometers, θ is Bragg's reflection angle, and β is the full width at half maximum (FWHM). The derived values for the average crystallite size of $MgCo_2O_4$ and $MgCo_2O_4$/MXene composites using eqn (1) are 49.67 and 31.44 nm, confirming the nanoparticle behavior of both materials.

Fourier transform infrared (FTIR) spectroscopy is a valuable analytical technique for determining the functional groups and vibrational and bond stretching functionalities on the surface of produced $MgCo_2O_4$/MXene are shown in Fig. 2(c). The FTIR spectrum of $MgCo_2O_4$/MXene shows absorption peaks with

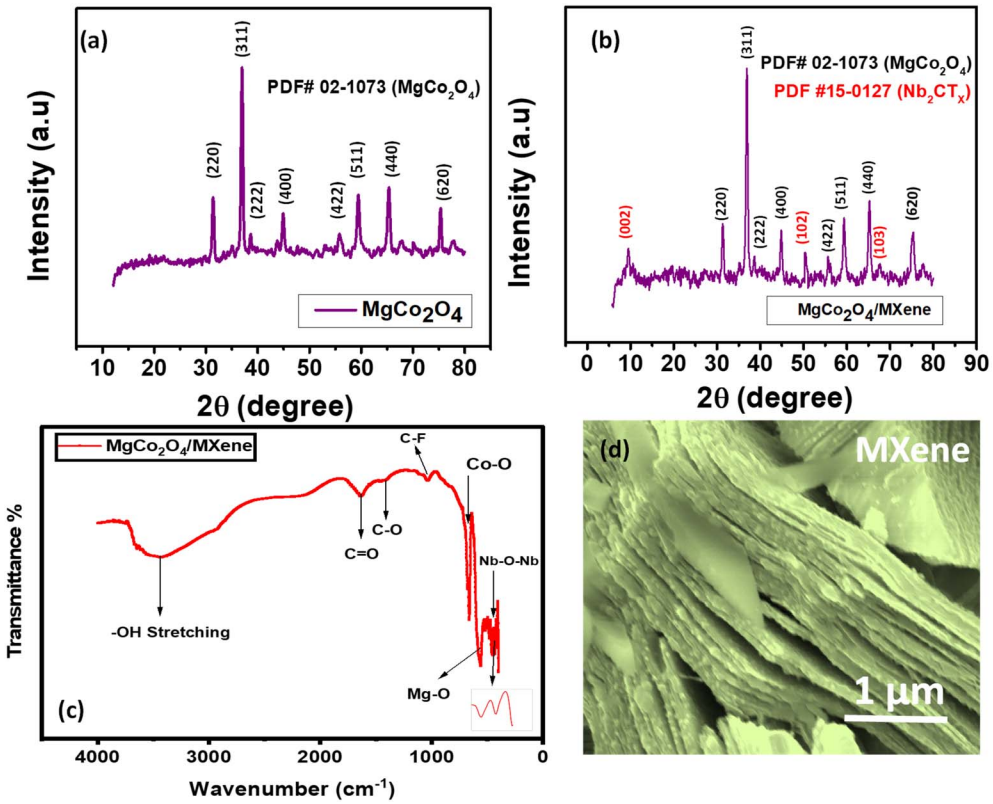

Fig. 2 XRD spectrum of the (a) $MgCo_2O_4$ and (b) $MgCo_2O_4$/MXene nanocomposites. (c) FTIR spectrum of $MgCo_2O_4$/MXene. (d) High-resolution SEM photograph of the accordion-like multilayered Nb_2CT_x MXene at 1 µm, confirming the successful etching of the Nb_2AlC MAX phase.

different wavenumbers, namely, 3439, 1631, 1411, 1029, 660 and 567 cm^{-1}. The absorption peak at 3439 cm^{-1} corresponds to the O–H (hydroxyl group) stretching vibration.[49] The C=O (carbonyl group) stretching vibrations are indicated by the peak position at 1631 cm^{-1},[35] whereas the C–O stretching vibrations are indicated by the peak at 1411 cm^{-1}.[50] The absorption peak at 1029 cm^{-1} is a feature of the C–F stretching mode.[51] The stretching vibration of Co–O is represented by the strong peak at 660 cm^{-1},[52] whereas the stretching vibration of Mg–O is shown by the peak at 567 cm^{-1},[53] proving the effective synthesis of Co_3O_4 and MgO. The band at 451 cm^{-1} corresponds to the symmetric stretching vibration of Nb–O–Nb.[54] The FTIR analysis confirms the presence of $MgCo_2O_4$ and Nb_2C in the sample of $MgCo_2O_4$/MXene.

Moreover, the morphological features of Nb_2CT_x are shown in Fig. 2(d). Clear multilayered (accordion-like) SEM pictographs of the Nb_2CT_x MXene can be seen in Fig. 2(d), which were taken at resolutions of 1 μm, respectively. This transformation shows that the layer of Al was successfully removed from Nb_2AlCT_x by HF etching, giving the Nb_2CT_x MXene its distinctive layered shape.

3.1.2 XPS. X-ray photoelectron spectroscopy (XPS) was employed to comprehensively determine the composition as well as to evaluate the oxidation states of the constituent elements in the $MgCo_2O_4$/MXene composite. A wide spectrum graph obtained from XPS showed in Fig. 3(a) presents a wide scan of the composite $MgCo_2O_4$/MXene over the binding energy range of 0–1400 eV, clearly revealing the presence of Mg, Co, Nb, O, and C. No more extra elemental peaks were observed, confirming the high compositional purity of the synthesized material. The Gaussian peak fitting was applied to precisely deconvolute the oxidation states of the constituent element.

The high-resolution XPS spectrum of Mg 1s (Fig. 3(b)) displays distinct deconvoluted peaks at binding energies of 1302.64 and 1304.4 eV, corresponding to the Mg^{2+} species associated with the Mg–O bonds in the oxide lattice. The small shift between these peaks can be explained by the differences in the chemical environment of the Mg^{2+} ion, such as coordination in the lattice of MgO or on the surfaces of MgO and $MgCo_2O_4$. Additionally, a peak at 1306.1 eV is attributed to the Mg–OH bond, confirming the presence of surface hydroxyl groups.[55–57]

The high-resolution XPS spectrum of Co 2p (Fig. 3(c)) exhibits two intense peaks corresponding to Co $2p_{3/2}$ (780.36) and Co $2p_{1/2}$ (796.3 eV) accompanied by a pair of satellite peaks. The distinct spin–orbit splitting of approximately 15.94 eV, along with the presence of satellite peaks, indicates the coexistence of Co^{2+} and Co^{3+} species, and it is attributed to the Co_3O_4 cubic phase.[58] The Co $2p_{3/2}$ spin–orbit doublet was deconvoluted into two peaks at 781.0 and 776.3 eV, corresponding to the Co^{2+} $2p_{3/2}$ and Co^{3+} $2p_{3/2}$ states, respectively. Similarly, the Co $2p_{1/2}$ doublet was split into different peaks at 792.43 and 796.74 eV, assigned to the Co^{2+} $2p_{1/2}$ and Co^{3+} $2p_{1/2}$ states. The appearance of satellite peaks near the Co 2p spin–orbit doublets, observed at a binding energy of 788.47 eV, further confirms the presence of cobalt oxide species.[59–61] Fig. 3(d) shows the high-resolution XPS spectrum of Nb 3d, where the deconvolution of Nb $3d_{5/2}$ and Nb $3d_{3/2}$ peaks at 206.05 and 207.31 eV confirms the Nb^{4+} and Nb^{+5} oxidation states. The deconvoluted peak at 205.05 eV is assigned to Nb–C bonding, whereas the 207.93 eV peak is ascribed to Nb–O interactions.[62,63]. Fig. 3(e) depicts high resolution spectrum of C 1s, with separated components upon deconvolution with a prominent peak at "284.75 eV" and 287.57 eV corresponds to sp^2-hybridized C–C/C=C bonds, and sp^3-hybridized C–O bonds respectively, representing surface functionalization and oxidation. One deconvoluted peak at 288.9 eV is also assigned to "O–C=O" (carbonyl/carboxyl, Co_3^{-2} species) functional groups, indicating the chemical modifications of carbon due to bonding with oxygen.[64,65]

Fig. 3(f) presents the O 1s XPS spectrum, which is further resolved into multiple distinct components. One deconvoluted peak name as O1 at 529.94 eV is corresponded to a characteristic metal–oxygen bond. Another deconvoluted O2 peak at 532.10 eV is typically associated with the adsorbed water molecules at or near the surface of the material, reflecting low oxygen coordination at defect sites. The O3 peak at 534.16 corresponds to oxygen-containing functional groups.[66–68] Fig. S3 depicts the high-resolution spectrum of F 1s with distinct peaks at 685.2 and 686.5 eV, attributed to the Nb–F and C–F bonds respectively, and thus, indicates surface terminations on the Nb_2C–T_x MXene. These surface terminations arise due to HF etching and confirm that this functionalized MXene leads to improved ion transportation, wettability and electrochemical performance of the composite. XPS analysis reveals that metals have multiple oxidation states, confirming the presence of rich redox-active sites in the $MgCo_2O_4$/MXene composite. Oxygen vacancies from the O 1s spectrum act as additional active sites for faradaic reactions and enhance ion diffusion. Moreover, the presence of oxygen-containing functional groups (C=O, O–C=O, and –OH) makes the surface more wettable, which makes electrolyte penetration easier and provides accessibility to active sites. The C 1s peak at 284.7 eV, attributed to the sp^2 carbon network of MXenes, exhibits high electrical conductivity, which lowers charge transfer resistance. All of these structural and chemical properties synergistically contribute to improved electrochemical performance, which leads to remarkable specific capacity, efficient ion transport, and long-term cycling stability.

3.1.3 Brunauer–Emmett–Teller (BET). The Brunauer–Emmett–Teller (BET) method was used to measure the specific surface area and adsorption characteristics of the synthesized $MgCo_2O_4$ and $MgCo_2O_4$/MXene composites using Nitrogen adsorption–desorption isotherms conducted at 77 K. As depicted in Fig. 4(a), both materials exhibit type IV isotherms with distinct hysteresis loops in the range of relative pressures (P/P_0), indicating the mesoporous nature according to the IUPAC. Adsorption at low P/P_0 values is due to the formation of a monolayer on the surface, and a sharp rise in the rate of adsorption at higher P/P_0 values is due to the capillary condensation in mesopores. A multipoint BET plot, which is constructed using linear regression of P/P_0 *versus* $1/[W(P/P_0 - 1)]$ (inset in Fig. 4(a)), shows good linearity, indicating that the BET model is valid in the range of selected pressures. At higher relative pressures ($(P/P_0 = 0 > 0.5)$), a noticeable divergence

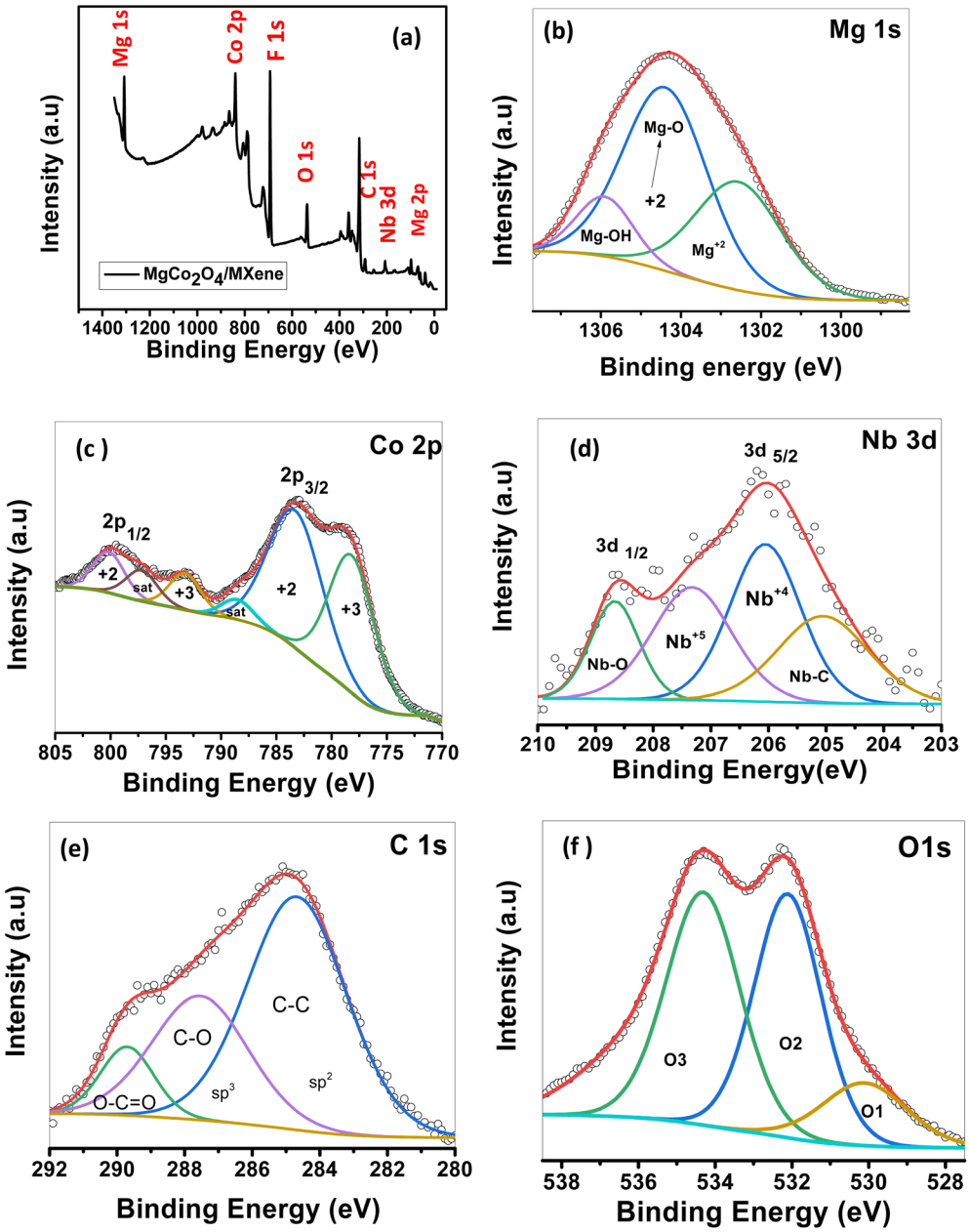

Fig. 3 (a) Wide-spectrum XPS graph of $MgCo_2O_4$/MXene. High-resolution spectra of the (b) Mg 2p, (c) Co 2p, (d) Nb 3d, (e) C 1s and (f) O 1s regions.

between the adsorption and desorption branches is observed, forming a hysteresis loop. The specific surface area of the materials was calculated using the multipoint BET method. From the BET analysis, it can be concluded that the specific surface area (93.87 $m^2\ g^{-1}$) of $MgCo_2O_4$/MXene is significantly higher than that of $MgCo_2O_4$, which only possesses a specific surface area of 60.25 $m^2\ g^{-1}$. Moreover, the monolayer adsorption capacity of $MgCo_2O_4$/MXene is significantly higher, at 21.28 $cm^3\ g^{-1}$, than that of $MgCo_2O_4$ which only possesses a monolayer adsorption capacity of 13.84 $cm^3\ g^{-1}$. The larger monolayer volume indicates more efficient adsorption of gases and more available surface active sites, which are highly desirable for applications such as those in electrochemical energy storage devices. Moreover, the pore size distribution and pore volume were obtained from the desorption branch using the BJH model. As illustrated in Fig. 4(b), $MgCo_2O_4$/MXene exhibits a higher pore volume than that of $MgCo_2O_4$. This is due to the presence of MXenes, which effectively hinder the agglomeration of nanoparticles and synergistically integrate with metal oxide components, thereby creating an interconnected mesoporous structure that enables effective penetration of electrolytes with shorter diffusion lengths. Consequently, the $MgCo_2O_4$/MXene composite demonstrates superior electrochemical performance, owing to its larger surface area, higher pore volume, and improved ion transport kinetics, leading to enhanced charge storage capability and capacitive behavior.

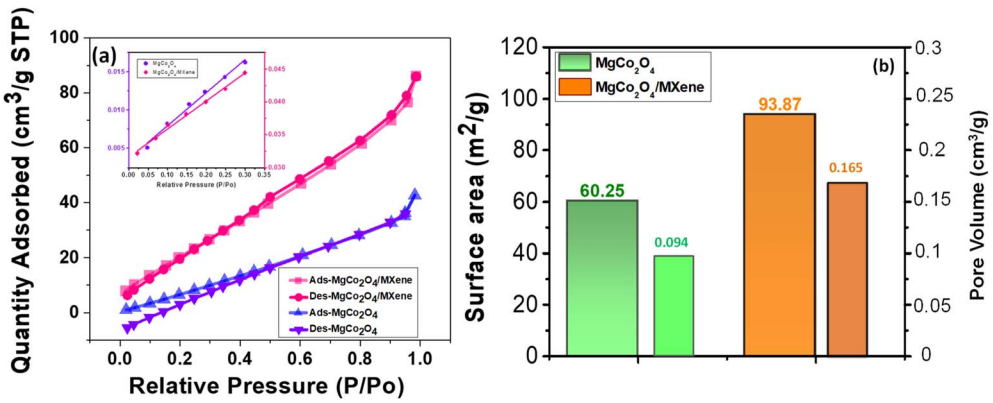

Fig. 4 (a) BET surface area isotherms (N_2 absorption and desorption) and (b) comparison of the surface area and pore volume of $MgCo_2O_4$ and $MgCo_2O_4$/MXene.

3.2 Morphological and elemental analysis

3.2.1 SEM and EDX. The morphological properties of the $MgCo_2O_4$ composite were identified by Scanning Electron Microscopy (SEM), and some of its images were captured under varying magnification powers (500 nm and 1 μm), as depicted in Fig. 5(a–c). From these micrographs, it is evident that the surface is made up of irregular-shaped microstructures with a rough texture.

The particles display non-uniform geometries and are tightly packed together to form a network throughout the material. Based on the morphological properties obtained from the images, there are indications of micro-scale features that are densely packed together. This indicates high roughness in this material. The material has an advantageous morphological structure for an electrode material as it will ensure high electrolyte diffusion into this material in addition to having high electrochemically active sites. Additionally, the interconnected particles will ensure high charge transfer in this material.

The elemental constituents of $MgCo_2O_4$ were also subjected to analysis using an energy-dispersive X-ray spectrometer, as depicted in Fig. 5(d). The analysis reveals that the material is composed of magnesium (Mg), cobalt (Co), and oxygen (O) without any detectable peak corresponding to impurities. This is an affirmation of the successful synthesis and compositional purity. These data are also consistent with the data obtained by X-ray diffraction analysis. Finally, the images obtained by elemental analysis using energy-dispersive X-ray spectroscopy

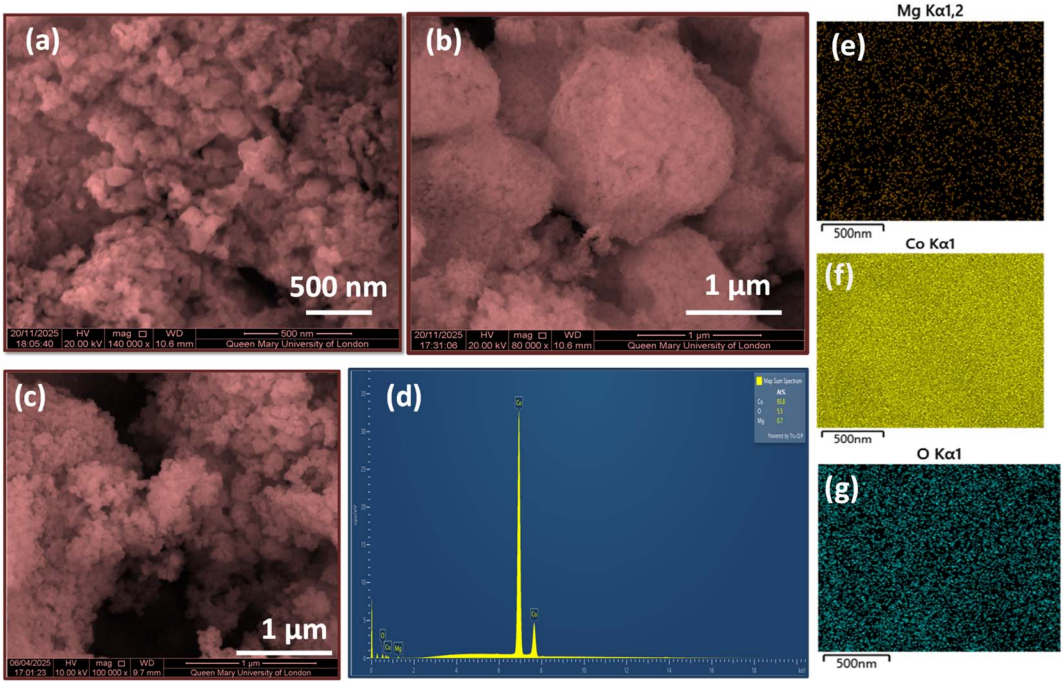

Fig. 5 (a–c) Scanning electron microscopy (SEM) pictographs of $MgCo_2O_4$ at high resolutions of 500 nm and 1 μm. (d) EDX spectrum of $MgCo_2O_4$ and (e–g) EDX elemental mapping images of the $MgCo_2O_4$ nanocomposite.

confirm that the elements are well distributed across the microstructure, as depicted in Fig. 5(e–g). Further analysis using the ImageJ software for the determination of average size from Fig. S1 shows that the size is approximately 71 nm, which is an affirmation that nanocomposites are evenly distributed.

Fig. 6(a–c) present the SEM images of the $MgCo_2O_4$/MXene composite at magnifications of 500 nm, 1 μm, and 2 μm, respectively. It can be noted from these images that the smaller sizes of $MgCo_2O_4$/MXene platelet-like nanostructures are evenly decorated on the MXene two-dimensional sheets with a well-integrated heterostructure. The individual nanoparticles display irregular nanosheet-like morphologies with even distribution on the two-dimensional Nb_2CT_x (MXene) substrate. Space among nanoparticles on MXene architecture helps to display an open surface texture, which facilitates easier access to the electrolyte.

The elemental composition of the obtained composite of $MgCo_2O_4$/MXene was determined by EDX spectroscopy, as displayed in Fig. 6(d). The EDX analytical result verifies the existence of magnesium (Mg), cobalt (Co), oxygen (O), niobium (Nb), and carbon (C), confirming the successful loading of composite $MgCo_2O_4$ on the MXene architecture. Fig. 6(e–i) present the corresponding EDX elemental mapping images for identifying the spatial distribution of individual elements on the composite surface, from which it could be found that all elements are evenly spread onto the composite surface, signifying the perfectly homogeneous distribution of all components. The lower intensity of Mg in the EDX spectrum is due to its lower atomic number, and also, EDX technique is less sensitive towards lighter elements. The identification of Mg in the composite material has been achieved through the XRD pattern and XPS spectrum, which indicate the successful synthesis of $MgCo_2O_4$. The quantification of particle sizes of the composite $MgCo_2O_4$/MXene could be performed using the ImageJ analysis software, as depicted graphically in Fig. S2, which reveals that the average size of the obtained composite is around 36 nm with significant reduction compared to bare $MgCo_2O_4$. The two-dimensional MXene substrate with a relatively large area and hydroxyl groups like –O, –F, and –OH helps to achieve even nucleation as well as control of particle sizes. So that $MgCo_2O_4$/MXene composite possesses reduced sizes with proper texture on its surface, possessing considerable benefits to display enhanced performance.

3.3 Electrochemical properties

3.3.1 Cyclic voltammetry analysis. The electrochemical analysis of $MgCo_2O_4$ and $MgCo_2O_4$/MXene was assessed using a series of cyclic voltammetry (CV), electrochemical active surface area (ECSA), galvanostatic charge discharge (GCD), and

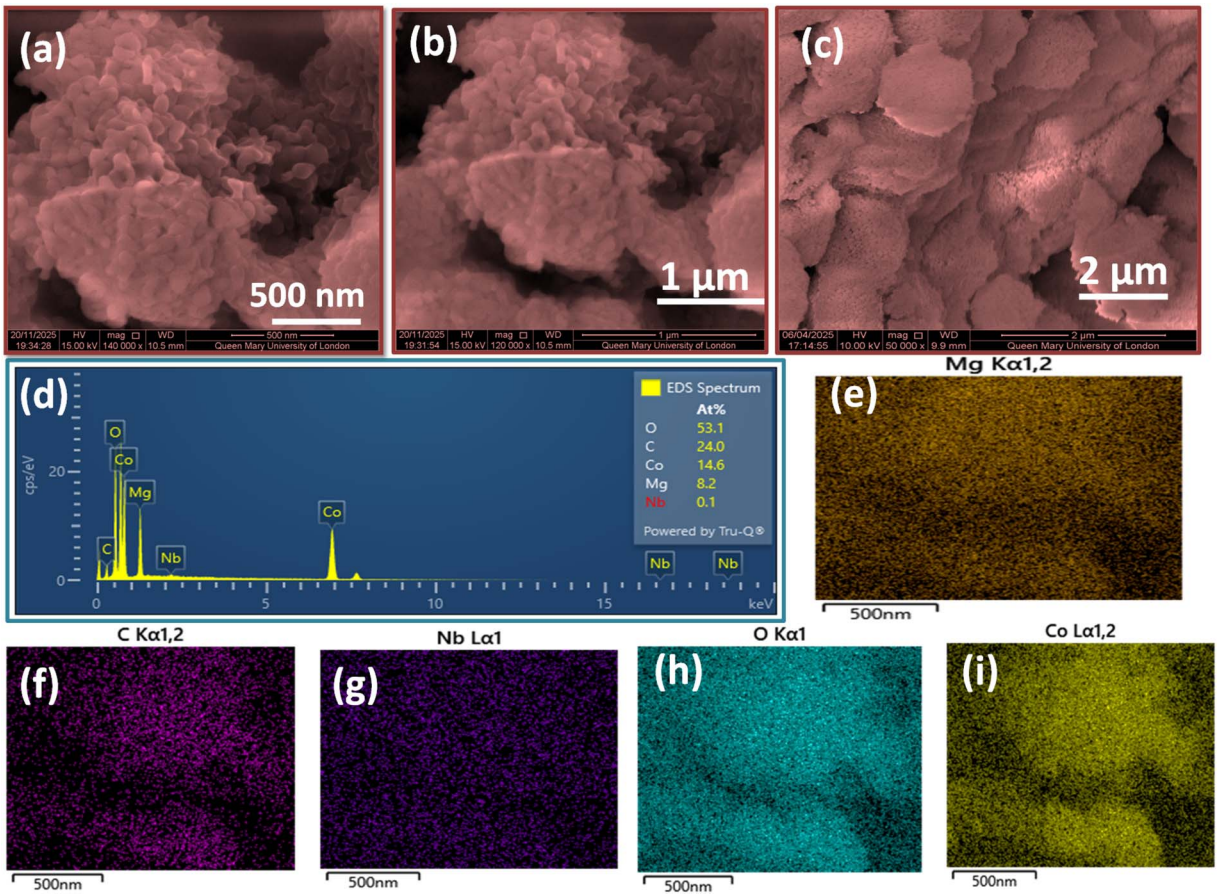

Fig. 6 (a–c) Scanning electron microscopy (SEM) pictographs of $MgCo_2O_4$/MXene at high resolutions of 500 nm, 1 μm and 2 μm respectively. (d) EDX spectrum of $MgCo_2O_4$/MXene. (e–i) EDX elemental mapping images of the $MgCo_2O_4$/MXene nanocomposite.

electrochemical impedance spectroscopy (EIS). Initially, CV was carefully used to assess the electrochemistry of both samples ($MgCo_2O_4$ and $MgCo_2O_4$/MXene) utilizing a three-electrode setup. In the three-electrode system, a platinum (Pt) wire served as the counter electrode, an Ag/AgCl electrode as the reference electrode, and the synthesized substance applied to a nickel (Ni) foam served as the working electrode. All of the prepared materials, MXene (Nb_2CT_x), $MgCo_2O_4$ and $MgCo_2O_4$/MXene, were measured within a potential window of 0.1–0.6 using cyclic voltammetry (CV) in a 3 M KOH electrolyte at scan rates of 10, 20, 30, 40, 50, and 100 mVs^{-1}. Fig. 7(a) shows that $MgCo_2O_4$/MXene shows a huge integrated area under the CV curve at 20 mVs^{-1} as compared to the MCO and Nb_2CT_x MXene, which leads to enhanced specific capacitance compared to the others. The CV curve of the Nb_2C MXene in the range of 0–0.6 V indicates the redox characteristics instead of having an ideal rectangular shape, suggesting the combination of EDL capacitance and pseudocapacitance behavior. These characteristics occur due to the presence of different functional groups (–O and –OH), giving rise to faradaic reactions.[69] So, significant pseudocapacitive behavior has been observed in (this potential window) surface-functionalized Nb_2C MXene while minimizing side reactions.

Fig. 7(b and c) display the related CV profiles, and the pseudocapacitive behavior is demonstrated by the distinct, sharp, oxidation and reduction peaks of $MgCo_2O_4$ and $MgCo_2O_4$/MXene. As the scan rates increase, the redox peaks exhibit a shift toward maximum potentials.

The small distortion and peak shifting at high scan rates may be attributed to slight polarization and ion diffusion limitations, which are typically characteristic of the pseudocapacitive material. At high scan rates, there is not enough time for the electrolytic ions to reach the active sites, resulting in greater peak separation and slight signal deviations. Nevertheless, the

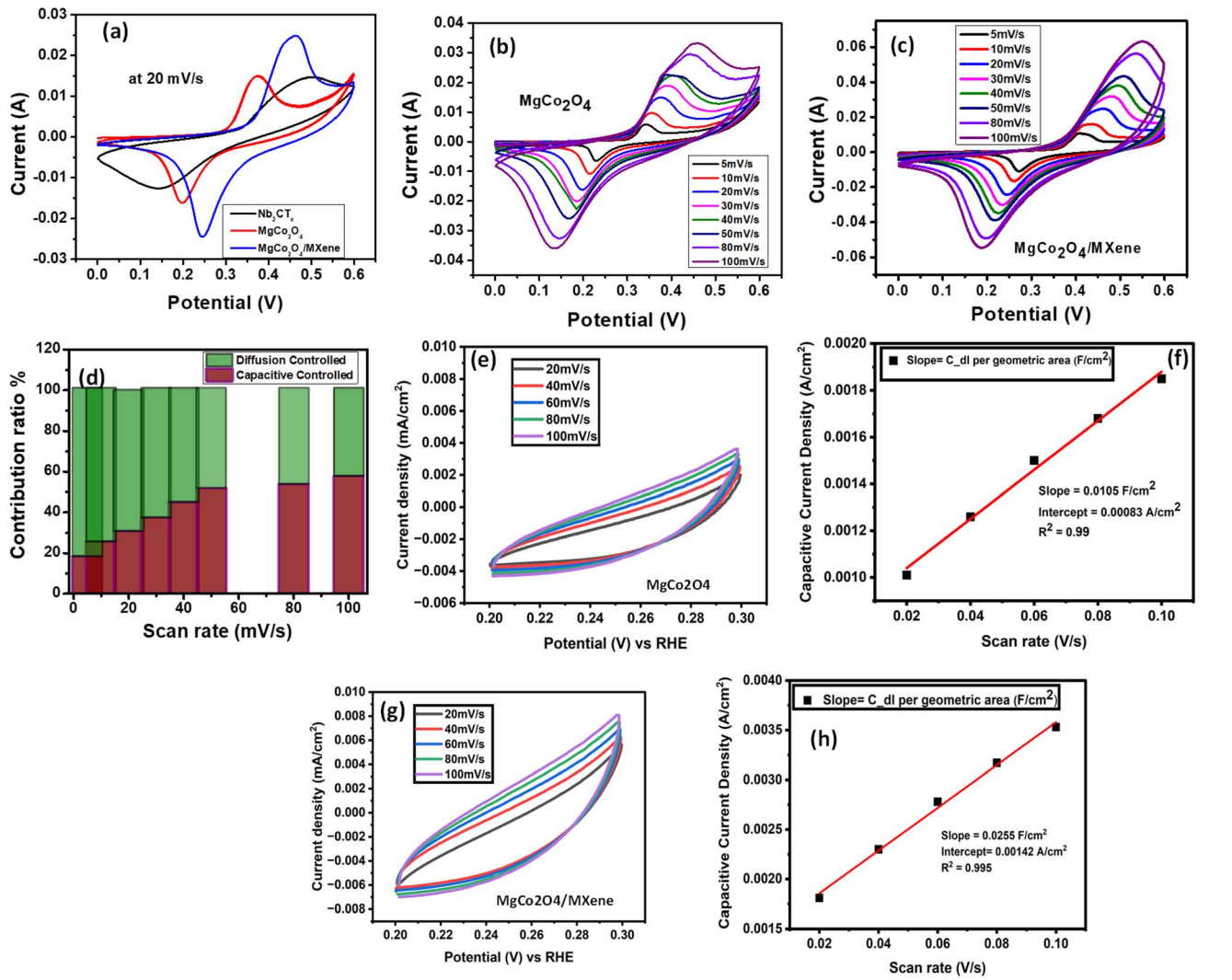

Fig. 7 (a) Comparison of the CV curves of Nb_2CT_x (MXenes), $MgCo_2O_4$, and $MgCo_2O_4$/MXene at 20 mVs^{-1}. CV curves of (b) $MgCo_2O_4$ and (c) $MgCo_2O_4$/MXene at different scan rates (5–100 mVs^{-1}). (d) Calibration of the diffusion and capacitive controlled contributions of $MgCo_2O_4$/MXene at multiple scan rates. CV curves of (e) $MgCo_2O_4$ and (g) $MgCo_2O_4$/MXene in the non-faradaic region and (f and h) their slope values for double-layer capacitances (C_{dl}), respectively.

clear redox peaks and smooth curves at low scan rates support the intrinsic and reliable electrochemical properties of the electrode.[70,71] CV curves are used to compute the specific capacitances of $MgCo_2O_4$ and $MgCo_2O_4$/MXene using the following equation:[72]

$$C_s = \frac{\int I \times dv}{m \times k \times (\Delta V)}, \quad (2)$$

where C_{sp} is the specific capacitance (F g^{-1}), m is the loading active mass (g), K is the scan rate (mV s^{-1}), ΔV is the potential window (V), and A is the integrated area ($V A$) of the CV curve in a single cycle. At scan rates of 5, 10, 20, 30, 40, 50, 80, and 100 mVs^{-1}, the calculated specific capacitances are 1075.8, 971.1, 860.3, 640.92, 590.25, 430.75, 370.80, and 330.32 F g^{-1} for $MgCo_2O_4$/MXene and 728.8, 668.9, 585.7, 424.9, 396.7, 306.7, 258.8, and 209.60 F g^{-1} for $MgCo_2O_4$, respectively. Compared to $MgCo_2O_4$, $MgCo_2O_4$/MXene exhibits a higher specific capacitance, which might be controlled by the presence of the Nb_2CT_x MXene.

The faradaic reaction involving Co^{4+}/Co^{3+} reactions is in charge of the redox peaks of the CV curve of $MgCo_2O_4$ and $MgCo_2O_4$/MXene, as shown in Fig. 7(b and c). Niobium carbide experiences redox reactions and surface hydroxylation to aid in charge storage, whereas magnesium oxide dissolves in an alkaline solution to produce hydroxylated species. The following are the expressions for the faradaic process:[73,74]

$$MgCo_2O_4 + 2H_2O \leftrightarrow 2CoOOH + Mg^{2+} + 2OH^-, \quad (3)$$

$$CoOOH + H_2O + e^- \leftrightarrow Co(OH)_2 + OH^-, \quad (4)$$

$$Nb_2C + 2OH^- \leftrightarrow Nb_2C(OH)_2 + 2e^-, \quad (5)$$

$$Nb_2C + 4OH^- \leftrightarrow 2NbO(OH) + 2H_2O + 4e^-, \quad (6)$$

$$NbO(OH) + e^- + OH^- \leftrightarrow NbO_2 + H_2O. \quad (7)$$

Different techniques have been reported to identify capacitive (non-diffusion-limited) and diffusion-controlled processes. In summary, Dunn provided a normalizing formula for CV kinetics analysis in 2007 that is found in eqn (8).[72] To calculate the contributions of the $MgCo_2O_4$/MXene electrode's capacitive and diffusion-controlled processes, eqn (8) was employed as given:[72]

$$i(v) = k_1 (V) + k_2 (V)^{1/2} = i \text{ (capacitive)} + i \text{ (diffusion)}, \quad (8)$$

where the symbols $i(v)$, k_1, k_2, and v represent the current (at a particular potential V), the contribution of the capacitive effect, the diffusion-controlled process, and the scan rate, respectively. The combined contributions of the capacitive and ion diffusion to the overall capacitance values are depicted graphically. The overall capacitance contributions of the $MgCo_2O_4$/MXene electrode at a scan rate of 20 mVs^{-1} are shown in Fig. 7(d). The electrode $MgCo_2O_4$/MXene exhibits diffusion-controlled contributions of 82.91%, 75.41%, 69.28%, 63.59%, 56.01%, 49.26%, 47.26%, and 43.13% at scan rates of 5, 10, 20, 30, 40, 50, 80, and 100 mVs^{-1}, respectively. From the quantitative study, it is evident that diffusion control occurs significantly when the scan rate is low, which indicates considerable faradaic ion intercalation. As the scan rate increases, there is an increased capacitive contribution due to the surface control kinetics. This behavior exhibits a hybrid charge storage mechanism involving both diffusion-controlled faradaic reactions and surface-driven pseudocapacitance, rather than a purely pseudocapacitive or purely battery-type behavior.

3.3.2 Electrochemical surface area (ECSA). First, we assessed the electrochemical capabilities of $MgCo_2O_4$ and $MgCo_2O_4$/MXene through electrochemical surface area (ECSA) using a three-electrode setup comprising a 3 M KOH electrolyte with the active material, Ag/AgCl, and graphite rod as the working, reference and counter electrodes, respectively. In the non-faradaic potential window, the ECSA was calculated using CV curves from the double-layer capacitance (C_{dl}). The CV curves of the prepared $MgCo_2O_4$/Mxene (0.20–0.30 V) at high scan rates of 20, 40, 60, 80, and 100 mVs^{-1} are illustrated in Fig. 7(e and g). Additionally, the capacitive current density (i_{cap}) values were calculated using the formula $|i_a - i_c|/2v$, where v indicates the applied scan rates (mVs^{-1}) and $|i_a - i_c|$ is the anodic and cathodic current density differences. The capacitive current density (i_{cap}, Acm^{-2}) was plotted *versus* scan rate (Vs^{-1}) and a linear fit yielded the slope = C_{dl} per geometric area (Fcm^{-2}), as shown in Fig. 7(f and h). The slope of the graph was used to calculate the double-layer capacitance (C_{dl}). After that, ECSA was calculated using the following equation:[75]

$$ECSA = C_{dl}/C_s \times A \text{ (geometrical)}, \quad (9)$$

where C_{dl} is the slope, A represents the geometrical area of the electrode surface, and C_s is the specific capacitance of a uniform surface composed of the same material, which is normally about 40 μF cm^{-2} for the majority of metal electrodes submerged in aqueous solutions. $MgCo_2O_4$/MXene achieves large C_{dl} and ECSA values of 25.5 mF cm^{-2} and 638 cm^2, respectively, which is higher than the values of 10.5 mF cm^{-2} and 263 cm^2 of $MgCo_2O_4$. Better electrolyte penetration and quicker ion/electron transfer are made possible by the large ECSA, which enhances the electrochemical performance of the composite in comparison to the base material.

3.3.3 Galvanostatic charge–discharge (GCD). As displayed in Fig. 8(a), the GCD measurements of Nb_2CT_x, $MgCo_2O_4$, and $MgCo_2O_4$/MXene electrodes were recorded over a potential window of 0–0.6 V and at a current density of 1 A g^{-1}. These curves provide information on the electrochemical attributes of each electrode under charge discharge conditions. Every electrode shows a nonlinear charge–discharge curve, which indicates a redox process where the diffusion process dominates, in support with the CV results, and validates the purely faradaic behavior of both materials.

Particularly, the $MgCo_2O_4$/MXene electrode shows the longest discharge time as compared to $MgCo_2O_4$, demonstrating its higher specific capacity. Based on the GCD curves, the specific capacitances for Nb_2CT_x, $MgCo_2O_4$, and $MgCo_2O_4$/MXene were found using eqn (10) within a possible window of 0–0.6 V to be 204.55, 749.78, and 1257.75 F g^{-1}, respectively, at

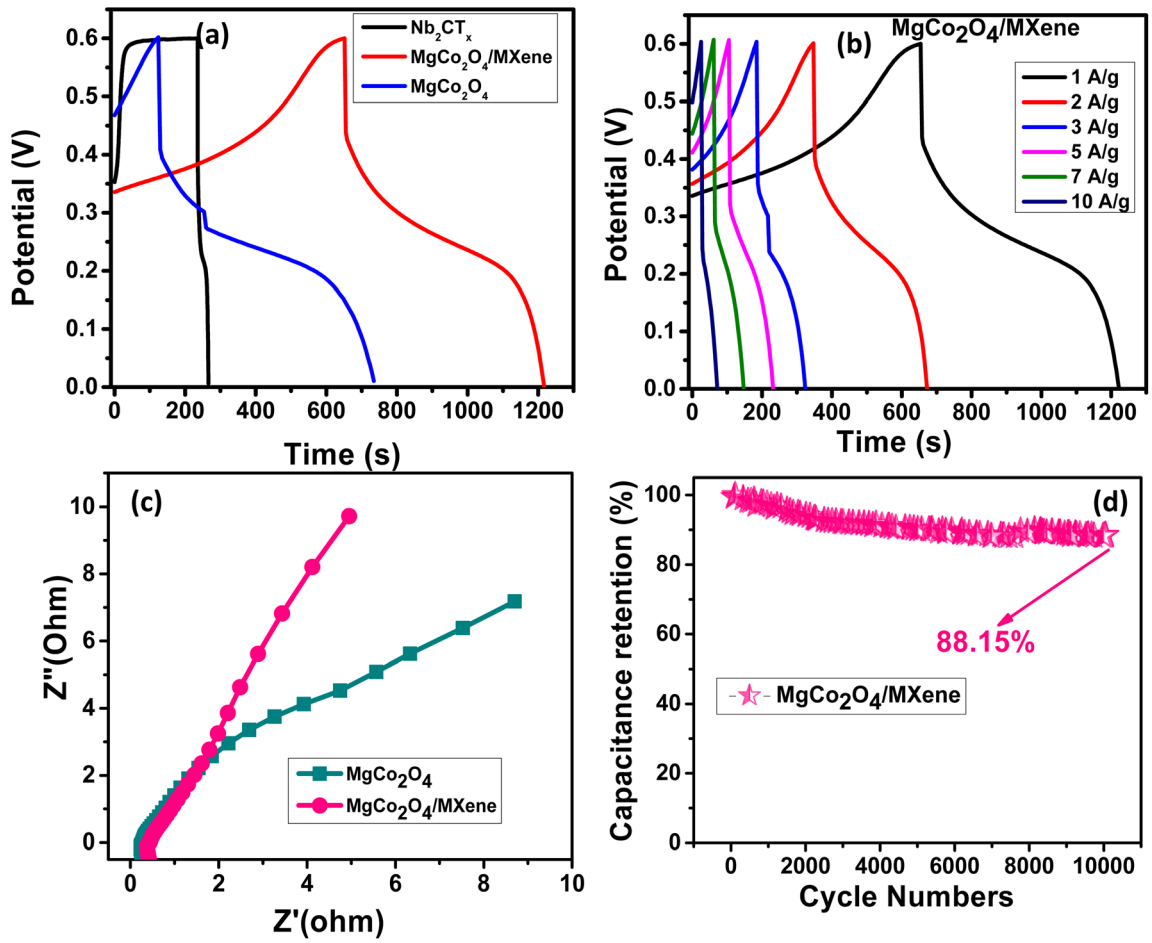

Fig. 8 (a) Comparison of the GCD curves of Nb_2CT_x, $MgCo_2O_4$ and $MgCo_2O_4$/MXene at 1 A g^{-1}. (b) GCD curves of $MgCo_2O_4$/MXene at multiple current densities ranging from 1 to 10 A g^{-1}. (c) Nyquist plots (obtained from EIS data) of $MgCo_2O_4$ and $MgCo_2O_4$/MXene. (d) Capacitance retention of $MgCo_2O_4$/MXene at 1 A g^{-1} over 10 000 charge discharge cycles.

1 A g^{-1}. The GCD curves of $MgCo_2O_4$/MXenes at various current densities 1, 2, 3, 5, 7, and 10 A g^{-1} within a potential window of 0–0.6 V are shown in Fig. 8(b). Eqn (10) is used to calculate the specific capacitance (C_s) using $MgCo_2O_4$/MXene GCD curves at different current densities[72] as follows:

$$C_{sp} = I_d \times T_d/\Delta V \times m, \quad (10)$$

where T_d stands for the discharge time (s), I_d for the discharge current (A), ΔV for the potential window (0.0–0.6 V), m for the active electrode loaded mass (g), and C_s for the specific capacitance (F g^{-1}). The specific capacity (C_{sp}) of $MgCo_2O_4$/MXene obtained from eqn (10) is 1257.75, 1040.2, 879.78, 803.39, 703.38 and 675 F g^{-1} at 1, 2, 3, 5, 7, and 10 A g^{-1}, respectively. The negligible IR drop in the GCD graph shows very low internal resistance, and hence, the calculation of capacitance is based on the complete discharge curve. The pristine $MgCo_2O_4$ electrode displays a slight IR drop owing to its lower electrical conductivity, while $MgCo_2O_4$/MXene demonstrates a negligible IR drop, which indicates higher charge mobility. One minor irregularity found in one discharge curve is considered to be associated with the temporary instability of measurements rather than the intrinsic behavior of the material. MXene incorporation in $MgCo_2O_4$/MXene composite, lower internal resistance and enhanced electrochemical performance, resulting more stable and symmetric GCD curves.

The specific capacitance of the $MgCo_2O_4$/MXene electrode gradually decreases as the current density increases. The nonlinearity and the apparent potential drops of the GCD curves at high current densities suggest that $MgCo_2O_4$/MXene nanocomposites lack sufficient active sites, which eventually cause the specific capacity to decrease from 1257.75 to 675 F g^{-1}. $MgCo_2O_4$/MXene shows a long discharge duration and high specific capacity because of the synergistic effect of $MgCo_2O_4$, and Nb_2CT_x, as well as the enhanced electrical conductivity, deep and effective electrolyte penetration, and large surface area provided by MXene layers. The specific capacitance of the nanocomposite $MgCo_2O_4$/MXene electrode in respect to current studies is summarized in Table 1.

To ensure material uniformity as well as data integrity during measurement, the resistive response of materials used for electrodes was studied using EIS (electrochemical impedance spectroscopy) in the frequency range of 0.1 to 10^5 Hz at 5 mV moderate amplitude. The Nyquist plot of both electrodes

Table 1 Comparison of the C_s values of $MgCo_2O_4$/MXene with those recently reported in the literature

Electrode	Current density (A g^{-1})	Specific capacitance	References
$MgCo_2O_4$	0.1 A g^{-1}	741 F g^{-1}	28
$MgCo_2O_4$/ZnS	1 A g^{-1}	919 F g^{-1}	76
$MgCo_2O_4$/MgO	1 A g^{-1}	1091 F g^{-1}	77
$MgCo_2O_4$/Ni_3S_2	1 A g^{-1}	1123.9 F g^{-1}	78
$MgCo_2O_4$/MXene	1 A g^{-1}	1257.75 F g^{-1}	Current work

is shown in Fig. 8(c), which typically consists of two parts: a semicircle in the high frequency band and an angled line in the low frequency range. The intercept on the real axis (Z') at a high frequency can be used to directly estimate the internal resistance (R_s), which is the sum of the inherent resistance, ionic resistance, and contact resistance of the electrolyte between the electrolyte and electrode materials.[79] The charge transfer resistance (R_{ct}) can be represented by the diameter of the semicircle at high frequencies during faradaic reactions.[80] Fig. S4 depicts the fitted plot of $MgCo_2O_4$ and $MgCo_2O_4$/MXenes with an employed circuit using the ZSimpWin software. In comparison to MCO (R_{ct} = 3.7 Ω), the $MgCo_2O_4$/MXene electrode has a comparatively low charge transfer resistance (R_{ct} = 1.9 Ω), suggesting that it performs better capacitively. Additionally, the low-frequency section of the Nyquist plot for $MgCo_2O_4$/MXene exhibits a steeper slope and a greater inclination toward the imaginary axis. As seen in Fig. 8(d), the $MgCo_2O_4$/MXene electrode material maintained a C_s value of up to 88.15% even after 10 000 cycles. Therefore, $MgCo_2O_4$/MXene is a better option due to its superior specific capacitance and outstanding capacitance retention, which render it a perfect electrode material for supercapacitor applications.

4 Ion transport properties

4.1 Ionic conductivity

One of the key factors in supercapacitor technology is the capability of ions to diffuse into a material, which helps in estimating the efficiency of the material in electrochemical reactions. Higher ionic conductivity helps in better diffusion of ions, thus allowing a larger number of oxidation–reduction reactions, thereby providing a better technique for the storage of charge. The ionic conductivity values for $MgCo_2O_4$ and $MgCo_2O_4$/MXene were obtained using the following equation:[81]

$$\sigma = \frac{L}{R_i \times A}, \quad (11)$$

where R_i is the ionic resistance, representing the resistance of the solution (R_s) determined from the EIS data, while L represents the thickness of the electrode, A denotes the cross-sectional area of the electrode, and σ indicates the ionic conductivity. From Table 2, it was observed that $MgCo_2O_4$/MXene has a high ionic conductivity of 1.79 × 10^{-3} S cm^{-1} compared to $MgCo_2O_4$, which has a relatively lower ionic conductivity of 1.12 × 10^{-3} S cm^{-1}.

4.2 Rate constant

The rate constant indicates the rate at which the reaction occurs and gives particular information about how quickly the electrons flow between the electrodes and ions in the electrolyte during the redox reaction. The rate constant is an ever-changing constant that has a very strong linkage with the charge transfer resistance. When the rate constant is large, it indicates that the redox reaction occurs very quickly, and hence, charge retention increases with faster power output and overall superior performances. The rate constant can be calculated using the following equation:[86]

$$\text{Rate constant}(k) = \frac{RT}{F^2 \times R_{ct} \times C}, \quad (13)$$

where (k) indicates that the rate constant, R indicates the universal gas constant with 8.314 J mol^{-1} k^{-1}, and T indicates the room temperature, respectively. On the other hand, the variables in the equation in the denominator indicate that F is the Faraday constant with 96 485C mol^{-1}, R_{ct} is the charge transfer resistance calculated by EIS, and C indicates the concentration of the electrolyte. From eqn (13), the rate constant values for $MgCo_2O_4$ and $MgCo_2O_4$/MXene electrodes are 2.40 × 10^{-5} cm s^{-1} and 4.67 × 10^{-5} cm s^{-1}, respectively. Increasing the rate constant indicates that the MXene plays an

Table 2 Comparison of the ion transport properties of $MgCo_2O_4$/MXene with those recently reported in the literature

Electrode	Ionic conductivity (σ)	Transference number (t_+)	Rate constant (k)	References
$BiMnO_3$/CNTs	0.978 × 10^{-3}	0.31	3.91 × 10^{-7}	82
$LaNiO_3$/MXene	6.3 × 10^{-3}	0.3	—	83
$BaCoO_3$/rGO	0.128	0.2	—	84
ZnO/CNTs	46.0 × 10^{-3}	0.01	6.49 × 10^{-7}	85
$MgCo_2O_4$/MXene	1.79 × 10^{-3}		4.67 × 10^{-5}	Current work

effective role in increasing the charge transfer rate between the electrolyte interfaces.

5 Conclusion

Thus, in conclusion, ultra-facile hydrothermal synthesis routes have been employed to synthesize the MXene, $MgCo_2O_4$, and the $MgCo_2O_4$/MXene nanocomposite. These samples have been structurally, morphologically, elementally, and functionally characterized. The enhanced electrochemical performance of the MXene-based nanocomposite can be attributed to the robust structure offered through the phase purity and defined crystalline structure replicated by the XRD results. There has been a significant alteration in the morphology of the composite of $MgCo_2O_4$ with the introduction of MXenes, where the size of the particles and the hybrid structure of the composite are smaller, as revealed by morphological characterizations. Moreover, the composite of $MgCo_2O_4$/MXene outperforms the pristine material of $MgCo_2O_4$ in terms of electrochemical performance through enhanced surface area, a greater number of active sites and shorter ion diffusion pathways. Based on electrochemical analysis, these $MgCo_2O_4$/MXene electrodes are pseudo-capacitive. $MgCo_2O_4$/MXene electrodes have the highest stability of 88.15% at 10 000 GCD cycles and a specific capacitance of 1257.75 F g^{-1} at 1 A g^{-1}. $MgCo_2O_4$/MXene had the lowest R_{ct} value, which can be ascribed to its superior conductivity, fast redox reactions, improved ion accessibility, and ion diffusion. This clearly exhibits that $MgCo_2O_4$/MXene is the best choice for use as a more promising material in supercapacitors.

6 Author contributions

Komal Ali Rao: writing original draft, conceptualization, formal analysis, investigation, methodology, data curation, software, supervision, validation, editing and review. Khizra Waheed: software, review and editing. Waqas Ahmad, Nokhaiz Naeem, and Muhammad Ehsan Mazhar: methodology and software. Muhammad Bilal, Muhammad Imran Khan, and Zahra Bayhan: resources and review.

Conflicts of interest

The authors declare that they have no known competing financial interests or personal relationships that could have appeared to influence the work reported in this paper.

Data availability

All data generated or analyzed during this study are included in this article. Furthermore, all related data are available from the authors upon request.

Acknowledgements

We express our gratitude to Princess Nourah bint Abdulrahman University Researchers Supporting Project number (PNURSP2026R452), Princess Nourah bint Abdulrahman University, Riyadh, Saudia Arabia.

References

1 P. Lamba, *et al.*, Recent advancements in supercapacitors based on different electrode materials: classifications, synthesis methods and comparative performance, *J. Energy Storage*, 2022, **48**, 103871.
2 S. Kumar, *et al.*, 0D to 3D carbon-based networks combined with pseudocapacitive electrode material for high energy density supercapacitor: A review, *Chem. Eng. J.*, 2021, **403**, 126352.
3 D.-G. Wang, *et al.*, Metal-organic framework-based materials for hybrid supercapacitor application, *Coord. Chem. Rev.*, 2020, **404**, 213093.
4 N. Fatima, *et al.*, Intercalation of carbonate ions into Ce-doped NiCoAl layered double hydroxides using accelerated kinetics for high-performance hybrid supercapacitor electrodes, *New J. Chem.*, 2026, **50**(3), 1562–1574.
5 F. Ahmad, *et al.*, Direct electron transfer chemistry of redox-active enzymes: applications in biosensor development, *Biofuel Bioprod. Biorefining*, 2025, **19**(3), 963–981.
6 S. Wu, *et al.*, An aqueous Zn-ion hybrid supercapacitor with high energy density and ultrastability up to 80 000 cycles, *Adv. Energy Mater.*, 2019, **9**(47), 1902915.
7 K. A. Rao, *et al.*, Development of NiCo2O4/rGO nanocomposites for high performance Supercapacitors, *Chem. Asian J.*, 2025, **20**(15), e00388.
8 S. S. Shah, *et al.*, Advanced strategies in electrode engineering and nanomaterial modifications for supercapacitor performance enhancement: A comprehensive review, *J. Energy Storage*, 2024, **79**, 110152.
9 L. Phor, A. Kumar and S. Chahal, Electrode materials for supercapacitors: A comprehensive review of advancements and performance, *J. Energy Storage*, 2024, **84**, 110698.
10 A. Irshad, *et al.*, Synergy of zero-dimensional carbon dots decoration on the one-dimensional architecture of Ag-doped V2O5 for supercapacitor and overall water-splitting applications, *Fuel*, 2024, **362**, 130705.
11 S. Samantaray, *et al.*, Unleashing recent electrolyte materials for next-generation supercapacitor applications: A comprehensive review, *J. Energy Storage*, 2023, **72**, 108352.
12 A. Mishra, *et al.*, Carbon cloth-based hybrid materials as flexible electrochemical supercapacitors, *ChemElectroChem*, 2019, **6**(23), 5771–5786.
13 G. Qi, *et al.*, High modulus carbon fiber based composite structural supercapacitors towards reducing internal resistance and improving multifunctional performance, *Compos. Sci. Technol.*, 2024, **254**, 110670.
14 K. Shireesha, *et al.*, Novel NiMgOH-rGO-based nanostructured hybrids for electrochemical energy storage supercapacitor applications: effect of reducing agents, *Crystals*, 2021, **11**(9), 1144.
15 S. Sarangapani, B. Tilak and C. P. Chen, Materials for electrochemical capacitors: theoretical and experimental constraints, *J. Electrochem. Soc.*, 1996, **143**(11), 3791.

16 G. Wang, L. Zhang and J. Zhang, A review of electrode materials for electrochemical supercapacitors, *Chem. Soc. Rev.*, 2012, **41**(2), 797–828.
17 N. Fatima, *et al.*, A surface oxygen-modified CoAlFe LDH@Fe 3 O 4-based high-performance supercapacitor: structural modification for improved electrochemical stability, *New J. Chem.*, 2026, **50**, 6125–6139.
18 C. Hao, *et al.*, Fabrication of flower-shaped CuCo2O4@MgMoO4 nanocomposite for high-performance supercapacitors, *J. Energy Storage*, 2021, **41**, 102972.
19 W. Abbas, *et al.*, Synergistic CuCo2O4/MWCNT nanocomposites: advanced electrode materials for energy storage and catalysis applications, *J. Mater. Sci. Eng.*, 2025, **20**(1), 96.
20 A. R. Patel, G. Sereda and S. Banerjee, Synthesis, characterization and applications of spinel cobaltite nanomaterials, *Curr. Pharm. Biotechnol.*, 2021, **22**(6), 773–792.
21 V. Jose, *et al.*, Spinel-based electrode materials for application in electrochemical supercapacitors–present status and future prospects, *Inorg. Nano-Met. Chem.*, 2022, **52**(12), 1449–1462.
22 S. G. Krishnan, *et al.*, Energy storage in metal cobaltite electrodes: Opportunities & challenges in magnesium cobalt oxide, *Renew. Sustain. Energy Rev.*, 2021, **141**, 110798.
23 J. Sun, *et al.*, Egg albumin-assisted hydrothermal synthesis of Co3O4 quasi-cubes as superior electrode material for supercapacitors with excellent performances, *Nanoscale Res. Lett.*, 2019, **14**(1), 340.
24 V. S. Kumbhar and D.-H. Kim, Hierarchical coating of MnO2 nanosheets on ZnCo2O4 nanoflakes for enhanced electrochemical performance of asymmetric supercapacitors, *Electrochim. Acta*, 2018, **271**, 284–296.
25 F. Liao, *et al.*, Solvothermal synthesis of porous MnCo2O4. 5 spindle-like microstructures as high-performance electrode materials for supercapacitors, *Ceram. Int.*, 2018, **44**(18), 22622–22631.
26 H. Gao, *et al.*, A general fabrication approach on spinel MCo2O4 (M= Co, Mn, Fe, Mg and Zn) submicron prisms as advanced positive materials for supercapacitor, *Electrochim. Acta*, 2018, **262**, 241–251.
27 Y. Y. Kannangara, *et al.*, The electrochemical performance of various NiCo2O4 nanostructures in hybrid supercapacitors: investigating the impact of crystalline defects, *J. Energy Storage*, 2024, **84**, 110717.
28 Z. Liu, *et al.*, Supercritical CO2-assisted solvothermal synthesis and characterization of MgCo2O4 nanospheres for high-performance capacitance, *Ceram. Int.*, 2024, **50**(5), 7789–7797.
29 A. M. Bogale, *et al.*, Structurally engineered MoS2@CuCo2O4 with palm-leaf morphology for button-type supercapacitor applications, *Mater. Sci. Semicond. Process.*, 2025, **200**, 109958.
30 M. M. Ghaziani, J. Mazloom and F. Ghodsi, Electrospun MgCo2O4 nanofibers as an efficient electrode material for pseudocapacitor applications: Effect of calcination temperature on electrochemical performance, *J. Phys. Chem. Solids*, 2021, **152**, 109981.
31 A. Lipatov, *et al.*, High electrical conductivity and breakdown current density of individual monolayer Ti3C2Tx MXene flakes, *Matter*, 2021, **4**(4), 1413–1427.
32 R. Khan, *et al.*, Transition metal dichalcogenides for next-generation supercapacitors: Recent advances, challenges, and future perspectives, *J. Alloys Compd.*, 2025, 182874.
33 T. Ramachandran, *et al.*, Black phosphorus as a multifunctional electrode material for all energy storage devices, *J. Alloys Compd.*, 2025, 182500.
34 T. Ramachandran, *et al.*, Beyond traditional MXenes: The promise of non-Ti MXenes in energy and catalysis, *Colloids Surf. A Physicochem. Eng. Asp.*, 2025, 137844.
35 S. Jayakumar, *et al.*, 2D (Ti3C2Tx) MXene: a comprehensive review of advancements in synthesis protocols, applications in supercapacitors, sustainability targets and future prospects, *J. Energy Storage*, 2024, **97**, 112741.
36 A. Tsyganov, *et al.*, Application of W 1.33 CT z MXenes obtained by hydrothermal etching as an additive to enhance the electrochemical energy storage properties of binder-free Ti 3 C 2 T x MXene films, *Dalton Trans.*, 2025, **54**(21), 8547–8558.
37 A. Tsyganov, *et al.*, Pseudocapacitive Behavior of Blade-Coated Mo1. 33CTx i-MXene Electrodes in Aqueous Electrolytes, *Nanomaterials*, 2025, **15**(20), 1593.
38 Y. A. Kumar, *et al.*, Double-transition metal MXenes for energy storage and conversion applications, *J. Power Sources*, 2026, **665**, 239027.
39 T. Ramachandran, *et al.*, A Layered Fe–SnO2/MXene Nanohybrid with 1225.6 F/g Capacitance and Long-Term Cycle Durability, *Mater. Chem. Phys.*, 2025, 131860.
40 S. Sagadevan, *et al.*, Exploring the potential of MXene-based aerogels and hybrid nanocomposites for supercapacitor applications, *J. Energy Storage*, 2024, **99**, 113269.
41 K. K. Garlapati, S. K. Martha and B. B. Panigrahi, VOx anchored Ti3C2Tx MXene heterostructures for high-performance 2.2 V supercapacitors, *J. Power Sources*, 2024, **605**, 234503.
42 X. Chen, *et al.*, Facile fabrication of CuCo 2 S 4 nanoparticles/MXene composite as anode for high-performance asymmetric supercapacitor, *Mater. Chem. Front.*, 2021, **5**(20), 7606–7616.
43 G. Guan and F. Guo, A review of Nb2CTx MXene: synthesis, properties and applications, *Batteries*, 2023, **9**(4), 235.
44 G. Guan, *et al.*, Nb2CT x MXene Anchored with Carbon Quantum Dots for Lithium-Ion Batteries, *ACS Appl. Nano Mater.*, 2023, **6**(24), 23620–23629.
45 D. Ponnalagar, Recent progress in two-dimensional Nb2C MXene for applications in energy storage and conversion, *Mater. Des.*, 2023, **231**(112046).
46 A. Tsyganov, *et al.*, Dielectric Properties of Flexible Poly (vinylidene fluoride) Nanocomposite Films with Two-Dimensional Nb2CTx MXene Filler, *J. Electron. Mater.*, 2025, **54**(12), 11333–11344.
47 K. A. Rao, *et al.*, Hydrothermal synthesis of bimetallic spinel MCo2O4/MXene (M= Ni, Zn) composites as efficient

supercapacitor electrodes, *Appl. Organomet. Chem.*, 2025, **39**(10), e70390.

48 W. Abbas, *et al.*, Study of the electrical properties and electrochemical sensing efficiency of hydrothermally synthesized Sr doped Nickel oxide nanomaterials, *Phys. Scr.*, 2022, **97**(7), 075004.

49 K. Agalya Priyadarshini, *et al.*, Biolarvicidal and pupicidal potential of silver nanoparticles synthesized using Euphorbia hirta against Anopheles stephensi Liston (Diptera: Culicidae), *Parasitol. Res.*, 2012, **111**(3), 997–1006.

50 D. B. Bailmare, P. Mangrulkar and A. D. Deshmukh, Designing copper containing MgCo2O4 nanosheet ultra-stable network for high performance asymmetric supercapacitors, *J. Energy Storage*, 2023, **59**, 106445.

51 H.-I. Kim, *et al.*, Effects of maleic anhydride content on mechanical properties of carbon fibers-reinforced maleic anhydride-grafted-polypropylene matrix composites, *Carbon Lett.*, 2016, **20**, 39–46.

52 L. Umaralikhan and M. Jamal Mohamed Jaffar, Green synthesis of MgO nanoparticles and it antibacterial activity, *Iran. J. Sci. Technol. Trans. A-Science*, 2018, **42**(2), 477–485.

53 G. Ren, *et al.*, Characterisation of copper oxide nanoparticles for antimicrobial applications, *Int. J. Antimicrob. Agents*, 2009, **33**(6), 587–590.

54 A. Calvo-Villoslada, *et al.*, Phase-Dependent Photocatalytic Activity of Nb2O5 Nanomaterials for Rhodamine B Degradation: The Role of Surface Chemistry and Crystal Structure, *Nanomaterials*, 2025, **15**(11), 846.

55 A. Velmurugan and A. R. Warrier, Production of biodiesel from waste cooking oil using mesoporous MgO-SnO2 nanocomposite, *J. Eng. Appl. Sci.*, 2022, **69**(1), 92.

56 G.-L. Song, *Corrosion of Magnesium Alloys*, Elsevier, 2011.

57 J. Bennet, *et al.*, Attestation in self-propagating combustion approach of spinel AFe2O4 (A= Co, Mg and Mn) complexes bearing mixed oxidation states: magnetostructural properties, *Appl. Surf. Sci.*, 2016, **383**, 113–125.

58 X. Wang, *et al.*, Effects of group IB metals of Au/Ag/Cu on boosting oxygen evolution reaction of cobalt hydroxide, *ChemCatChem*, 2023, **15**(7), e202300033.

59 Q. Huang, *et al.*, Direct fabrication of lamellar self-supporting Co3O4/N/C peroxymonosulfate activChem. Eng. J.ation catalysts for effective aniline degradation, *Chem. Eng. J.*, 2017, **313**, 1088–1098.

60 G. Arunkumar, *et al.*, Silver-integrated cobalt hydroxide hybrid nanostructured materials for improved electrocatalytic oxygen evolution reaction, *New J. Chem.*, 2024, **48**(4), 1671–1677.

61 R. Tholkappiyan and K. Vishista, Tuning the composition and magnetostructure of dysprosium iron garnets by Co-substitution: An XRD, FT-IR, XPS and VSM study, *Appl. Surf. Sci.*, 2015, **351**, 1016–1024.

62 S. Martínez-Méndez, *et al.*, Catalytic properties of silica supported titanium, vanadium and niobium oxide nanoparticles towards the oxidation of saturated and unsaturated hydrocarbons, *J. Mol. Catal. A: Chem.*, 2006, **252**(1–2), 226–234.

63 K. A. Rao, *et al.*, Nb 2 CT x MXene integrated DyMn 2 O 5 composites: tailored particle size and enhanced capacitance for high performance pseudocapacitors, *J. Mater. Chem. C*, 2025, **13**, 13803–13819.

64 A. Ermolieff, *et al.*, XPS, Raman spectroscopy, X-ray diffraction, specular X-ray reflectivity, transmission electron microscopy and elastic recoil detection analysis of emissive carbon film characterization, *Surf. Interface Anal.*, 2001, **31**(3), 185–190.

65 A. Kirakosyan, *et al.*, Poly (styrene sulfonic acid)-grafted carbon black synthesized by surface-initiated atom transfer radical polymerization, *Molecules*, 2023, **28**(10), 4168.

66 C. An, *et al.*, Porous NiCo2O4 nanostructures for high performance supercapacitors via a microemulsion technique, *Nano Energy*, 2014, **10**, 125–134.

67 L. Liu, *et al.*, Self-Assembled 3D Foam-Like NiCo2O4 as Efficient Catalyst for Lithium Oxygen Batteries, *Small*, 2016, **12**(5), 602–611.

68 G. Rekha, *et al.*, Systematic study on surface and magnetostructural changes in Mn-substituted dysprosium ferrite by hydrothermal method, *Appl. Surf. Sci.*, 2016, **385**, 171–181.

69 U. Ahmed and G. Nabi, Nonhazardous in-situ exfoliation approach for Ce-Nb2CTx MXene as highly stable pseudocapacitors electrode material applications, *J. Environ. Chem. Eng.*, 2025, **13**(2), 115949.

70 H. Gao, *et al.*, Facile construction of a MgCo 2 O 4@ NiMoO 4/NF core–shell nanocomposite for high-performance asymmetric supercapacitors, *J. Mater. Chem. C*, 2019, **7**(42), 13267–13278.

71 C. Miao, *et al.*, Facile synthesis of metal–organic framework-derived CoSe2 nanoparticles embedded in the N-doped carbon nanosheet array and application for supercapacitors, *ACS Appl. Mater. Interfaces*, 2020, **12**(8), 9365–9375.

72 K. A. Rao, M. E. Mazhar and J. Ahmad, Facile hydrothermal synthesis of a tri-metallic Cu–Mn–Ni oxide-based electrochemical pseudo capacitor, *Dalton Trans.*, 2024, **53**(31), 13012–13021.

73 P. Mohana, *et al.*, Facile Synthesis of Ni-MgO/CNT Nanocomposite for Hydrogen Evolution Reaction, *Nanomaterials*, 2024, **14**(3), 280.

74 Y. Teng, *et al.*, One-Step Controllable Synthesis of Mesoporous MgCo2O4 Nanosheet Arrays with Ethanol on Nickel Foam as an Advanced Electrode Material for High-Performance Supercapacitors, *Chem. Eur J.*, 2018, **24**(56), 14982–14988.

75 F. Ahmad, *et al.*, A highly active, low-cost CoZn ferrite electrocatalyst in oxygen reduction reactions, *Results Chem.*, 2025, **14**, 102095.

76 T. A. Sandosh and A. Simi, Facile and cost-effective ctab templated hydrothermal synthesis and characterization of MgCo2O4 electrode material for supercapacitor application, *J. Inorg. Organomet. Polym. Mater.*, 2021, **31**(1), 251–260.

77 M. W. Alam, *et al.*, Enhanced electrodes for supercapacitor applications prepared by hydrothermal-assisted nano sheet-shaped MgCo2O4@ ZnS, *Crystals*, 2022, **12**(6), 822.
78 J. Bhagwan and J. I. Han, High-performance asymmetric supercapacitor of sol-gel routed MgCo2O4/MgO microfiber, *J. Energy Storage*, 2024, **94**, 112463.
79 H. Chen, *et al.*, Facile synthesis of porous Mn-doped Co3O4 oblique prisms as an electrode material with remarkable pseudocapacitance, *Ceram. Int.*, 2019, **45**(6), 8008–8016.
80 M. Cheng, *et al.*, Interconnected hierarchical NiCo 2 O 4 microspheres as high-performance electrode materials for supercapacitors, *Dalton Trans.*, 2017, **46**(28), 9201–9209.
81 K. A. Rao, *et al.*, Interfacial ion diffusion and rapid charge transfer kinetics of the hydrothermally synthesized heterostructured Bi 2 WO 6/Bi 2 O 3/MXene composite for next-generation pseudocapacitors, *RSC Adv.*, 2026, **16**(13), 11779–11792.
82 S. Fatima, *et al.*, Microstructural tailoring for enhanced response of carbon nanotube-filled BiMnO3 electrodes, *Mater. Chem. Phys.*, 2025, 131198.
83 A. Shakoor, *et al.*, Synergistic Improvements in Ionic Conductivity, Diffusion Dynamics, and Transference Numbers for LaNiO3/MXene Supercapacitor Electrodes, *Batter. Supercaps*, 2025, 2500014.
84 M. Shahzad, *et al.*, Tuning diffusion coefficient, ionic conductivity, and transference number in rGO/BaCoO 3 electrode material for optimized supercapacitor energy storage, *RSC Adv.*, 2025, **15**(8), 6308–6323.
85 A. Hussain, *et al.*, Synergistically tailored ionic conduction and transport in ZnO/CNTs based electrodes with enhanced electrochemical efficiency in supercapacitors, *Electrochim. Acta*, 2025, 146736.
86 A. Shahzad, *et al.*, Investigating electrochemical properties in CNT-modified MoS2/Se composites for supercapacitor electrodes, *J. Power Sources*, 2025, **656**, 238067.